Journal of Electroanalytical Chemistry 716 (2014) 8–15

Contents lists available at ScienceDirect

Journal of Electroanalytical Chemistry

journal homepage: www.elsevier.com/locate/jelechem

On the improvement of photoelectrochemical performance and finite element analysis of reduced graphene oxide–$BiVO_4$ composite electrodes

Hyun S. Park [a], Hyung-Wook Ha [b], Rodney S. Ruoff [b], Allen J. Bard [a,*]

[a] Center for Electrochemistry, Department of Chemistry and Biochemistry, The University of Texas at Austin, Austin, TX 78712, United States
[b] Department of Mechanical Engineering and the Materials Science and Engineering Program, The University of Texas at Austin, Austin, TX 78712, United States

ARTICLE INFO

Article history:
Available online 8 September 2013

Keywords:
Photoelectrochemistry
Photocatalyst
Water splitting
Finite element analysis
Graphene
Bismuth vanadate

ABSTRACT

Incorporation of thermally reduced graphene oxide (RG-O) into the metal oxide semiconductor $BiVO_4$ improves its photoactivity by about three times for sulfite oxidation. The enhancement of photoactivity is attributed to reduced electron–hole recombination of $BiVO_4$ using the RG-O as a conductive matrix in the composite photocatalyst. Photoelectrochemical behavior of the $BiVO_4$ and RG-O/$BiVO_4$ composite electrodes were simulated using finite element analysis to obtain the carrier mobility and its lifetime in the photoelectrodes. In contrast with sulfite oxidation, the improvement of photocurrent for water oxidation of RG-O/$BiVO_4$ composite electrode was not significant because of the slower kinetics for water oxidation. To address the kinetic limitations, platinum (Pt) as an effective electrocatalyst was photodeposited on the RG-O/$BiVO_4$ electrode. Addition of the Pt significantly improved water oxidation photocurrent of the Pt/RG-O/$BiVO_4$ electrode. RG-O/W–Mo-doped $BiVO_4$ composite electrodes were also prepared to investigate a further enhancement of photoactivity of W–Mo-doped $BiVO_4$. The behavior obtained from RG-O/W–Mo-$BiVO_4$ and RG-O/$BiVO_4$ electrodes provides a valuable insight into the role of RG-O as a conducting additive and the role of W and Mo as dopants into $BiVO_4$.

1. Introduction

Metal oxide semiconductors, e.g., TiO_2, Fe_2O_3, WO_3 and $BiVO_4$, have been extensively studied as water oxidation photocatalysts for the possible solar photolysis of water [1]. Metal oxide semiconductors are chemically stable, cheap and abundant, and their semiconducting properties, such as the size of band-gap, the band-edge locations, and the carrier mobility, can be significantly modified by the addition of dopant, e.g., Si-doped Fe_2O_3 [2], N-doped WO_3 [3], and W-doped $BiVO_4$ [4,5]. However, significant electron–hole recombination, indicated by the short minority carrier-lifetime and short carrier-diffusion length of metal oxide semiconductors remains a major barrier to achieving a high conversion efficiency of sunlight to chemical energy, i.e., for hydrogen production by water splitting [6–8]. Methods of increasing the carrier mobility, e.g., by doping or the addition of conductive or electron accepting materials into the metal oxide semiconductor have been recently attempted to address the rapid electron–hole recombination of the photocatalysts. For example, conductive $TiSi_2$ was incorporated into TiO_2 [9,10], WO_3 [11], and α-Fe_2O_3 [12] to improve the electron transport through the electrodes. Also, composite photocatalysts with carbon based conducting materials, such as carbon nanotube or reduced graphene oxide (RG-O), have also been suggested for TiO_2 [13–15] and $BiVO_4$ [16] to overcome the rapid recombination of excited electron–hole pairs; the addition of conductive materials into semiconductors increases the rate at which electrons are transported from the semiconductor/solution interface and hence the separation of electron–hole pairs. However, conductive materials can also act as traps, i.e., recombination centers for the electron–hole pairs [17].

The chemistry of graphite oxide (GO) and later graphene oxide (G-O) has been extensively studied for its properties and synthesis since the first report of GO in 1859 [18]. G-O is intrinsically an insulator, but it is used as a precursor for graphene-like material, i.e., reduced graphene oxide (RG-O). G-O is a possible source for the mass production of RG-O, and chemical derivatives of G-O and RG-O are promising materials for such applications as polymer nanocomposites, ultracapacitors, rechargeable batteries, sensors, and thin films [19–23]. Among such applications, RG-O (or G-O) composites with semiconductor photocatalysts have been reported to enhance photoactivity with the RG-O as a conductive additive to improve the bulk conductivity and facilitate electron–hole separations in photocatalysts as described above [14–16]. Here, we report the facile preparation and photoelectrochemical (PEC) behavior of RG-O/metal oxide composite photocatalysts based on $BiVO_4$ and W–Mo-doped $BiVO_4$. We also report a simulation (finite element analysis) of the PEC properties [24–26]. $BiVO_4$, with a band gap

* Corresponding author. Tel.: +1 512 471 3761.
E-mail address: ajbard@mail.utexas.edu (A.J. Bard).

1572-6657/$ - see front matter © 2013 Elsevier B.V. All rights reserved.
http://dx.doi.org/10.1016/j.jelechem.2013.08.036

of 2.4 eV, is a visible light water oxidation photocatalyst. Moreover, W-doped $BiVO_4$ or W–Mo-doped $BiVO_4$ produces a photocurrent for water oxidation that is more than 10 times higher than undoped $BiVO_4$ [4,5]. $BiVO_4$ or W–Mo-doped $BiVO_4$, were employed in a simple two-step process to fabricate composite electrodes in which G-O is exfoliated and homogenously dispersed ultrasonically in ethylene glycol solution and then thermally reduced during metal oxide formation by thermal annealing of drop-cast electrodes in air. In addition, in some experiments a Pt electrocatalyst was photodeposited onto the composite electrodes to decrease kinetic limitations of the water oxidation reaction on the composite electrodes; the effect of reduced electron–hole recombination by incorporation of RG-O clearly results in an increased photocurrent after the surface treatment.

2. Experimental

2.1. Chemicals

$Bi(NO_3)_3{\cdot}5H_2O$ (99.999%) and $(NH_4)_{10}H_2(W_2O_7)_6{\cdot}xH_2O$ (99.99%) were obtained from Strem Chemicals (Newburyport, MA). H_2SO_4 (98%), HCl (Technical grade), $KMnO_4$ (99.6%), Na_2HPO_4 (99.9%), NaH_2PO_4 (99.5%), MeOH (99.8 %), and ethylene glycol were purchased from Fisher Scientific (Pittsburg, PA). H_2O_2 (30 wt% in water), $H_2PtCl_6{\cdot}xH_2O$ (99.9%), $(NH_4)_6Mo_7O_{24}{\cdot}4H_2O$ (99.98%), and Na_2SO_4 (99.0%) were purchased from Sigma–Aldrich (St. Louis, MO). VCl_3 (99%, Alfa-Aeser, Ward Hill, MA) and Na_2SO_3 (99.6%, Mallinckrodt Baker, Phillipsburg, NJ) were used as received. Fluorine-doped tin oxide (FTO, TEC 15, Pilkington, Toledo, OH) was used as a substrate of the electrodes. Deionized (DI) Milli-Q water was used as the solvent in electrochemical experiments.

2.2. Graphene oxide (G-O) preparation

Graphite oxide (GO) was synthesized by a modified Hummer's method [27]. Briefly, 100 mg of natural graphite (SP-1, Bay Carbon, Bay City, MI) was mixed with 50 mL concentrated H_2SO_4 in a flask, followed by the addition of 500 mg of $KMnO_4$. After addition of $KMnO_4$, the mixture was heated at 35 °C and stirred for 2 h. Excess DI water (50 mL) was added to the flask (placed in an ice bath), and then more water (100 mL) was added followed by stirring in the ice bath for 1 h. H_2O_2 (30 wt% in water) was then added to the mixture until no further gas evolution was observed, followed by stirring for 2 h. The final suspension was filtered and washed with HCl (10% in water) and dried in air. Suspensions of G-O platelets were prepared using an ultrasonic bath (2510R-MT, Bransonic, Danbury, CT) by sonication of GO in DI water or ethylene glycol for 1 h.

2.3. Electrodes

Thin film electrodes of the $BiVO_4$ (or $BiVO_4$ with 2 atomic% (at%) W and 6 at% Mo, 'W–Mo-doped $BiVO_4$') and RG-O/$BiVO_4$ (or RG-O/W–Mo-doped $BiVO_4$) composites were prepared on an FTO substrate by drop casting the precursor solution. The metal oxide films were cast using 100 μL of a precursor solution with a total concentration of 20 mM in ethylene glycol. For RG-O/metal oxide composite electrodes, the targeted amount of GO powder was suspended in the metal oxide precursor solution and the solution was ultrasonicated for 1 h before drop casting. Then, the film was annealed in air for 3 h at temperatures from 400 °C to 550 °C, ramped from room temperature at a rate of 1 °C per min.

Photodeposition of Pt on photoelectrodes was conducted in aqueous solution of 10 mM H_2PtCl_6 and 0.2 M MeOH. $BiVO_4$ (and W–Mo-doped $BiVO_4$) and its RG-O composite electrodes on FTO were placed in the Pt precursor solution in a borosilicate glass cell. UV–visible irradiation was then performed at full output with a Xenon lamp (XBO 150 W, Osram, Munich, Germany) for 30 min, and a beam intensity was about 200 mW cm^{-2}. During the irradiation, photoreduction of Pt occurred on the thin film electrodes while MeOH was oxidized by the photoexcited electron and hole [28].

2.4. Instruments

A CH Instruments Model 630D electrochemical analyzer (Austin, TX) was used as a potentiostat for the experiments with the thin film electrodes. Illumination was with a Xenon lamp (XBO 150 W, Osram) at full output for UV–visible irradiation or using a 420 nm cut-off filter (WBF-3, Oriel, Darmstadt, Germany) for visible irradiation. A Pt gauze counter electrode and Ag/AgCl reference electrode in a saturated KCl solution were used to complete the three-electrode configuration. However, all potentials reported here are with respect to the normal hydrogen electrode (NHE). X-ray diffraction (XRD) measurements were performed using a Bruker–Nonius D8 advanced powder diffractometer (Madison, WI) operated at 40 kV and 40 mA with Cu Kα radiation (λ = 1.54 Å). Grazing incidence XRD (GIXRD) with incidence angle of 1° in detector scan mode was performed to obtain diffractograms from the thin film electrodes on FTO. The scan rate was 12° per minute in 0.02° increments of 2θ from 15° to 80°. Scanning electron microscopy (SEM) images were obtained with a LEO 1530 SEM at a working voltage of 10 kV and working distance of 5 mm. Thermogravimetric analysis (TGA) was conducted from room temperature to 800 °C with a Perkin–Elmer TGA 4000 with a ramp rate of 1 °C per min under dry air flow. X-ray photoelectron spectroscopy (XPS) was performed on a Kratos Axis Ultra DLD instrument (Manchester, UK) with a monochromatic Al X-ray source with 180° hemispherical electron energy analyzer.

2.5. Simulations

Finite element analysis was performed using COMSOL Multiphysics v.3.5 software (Burlington, MA) to study the photoanode properties. The steady state Poisson equation (Eq. (1)) and Nernst–Planck equations (Eqs. (3) and (4)) were used to calculate the potential distribution and the electron–hole transport in the semiconductor electrodes. The physics and reactions used in the simulations are schematically summarized in Fig. 1.

$$d(-\varepsilon_0\varepsilon_r d\psi/dx)/dx = \rho \quad (1)$$

where ε_0 is the vacuum permittivity, ε_r is the relative permittivity, ψ is the potential (of Fermi level vs vacuum level), and ρ is the excess charge density. The simulation domain and constants were set as shown in Supporting information Fig. S1; ρ was defined as

$$\rho = (C_p + C_n - N_d)q \quad (2)$$

where q is the electron charge, N_d is the fixed electron doping density at thermal equilibrium, and C_n and C_p is the local carrier density of electrons and holes, respectively. C_n and C_p were determined using the Nernst–Planck equations as shown below.

$$d(-D_n dC_n/dx + \mu_n C_n d\psi/dx)/dx = -R + G \quad \text{for} \quad C_n \quad (3)$$

$$d(-D_p dC_p/dx - \mu_p C_p d\psi/dx)/dx = -R + G \quad \text{for} \quad C_p \quad (4)$$

where D_n and D_p are the diffusion coefficients of electron and hole, and μ_n and μ_p are the mobilities for electrons and holes, respectively. The diffusion coefficient and mobility are related by the Einstein relation.

$$D_{n/p} = \mu_{n/p} kT/q \quad (5)$$

where k is the Boltzmann constant and T is the temperature. R is the electron–hole recombination rate in the bulk semiconductor and

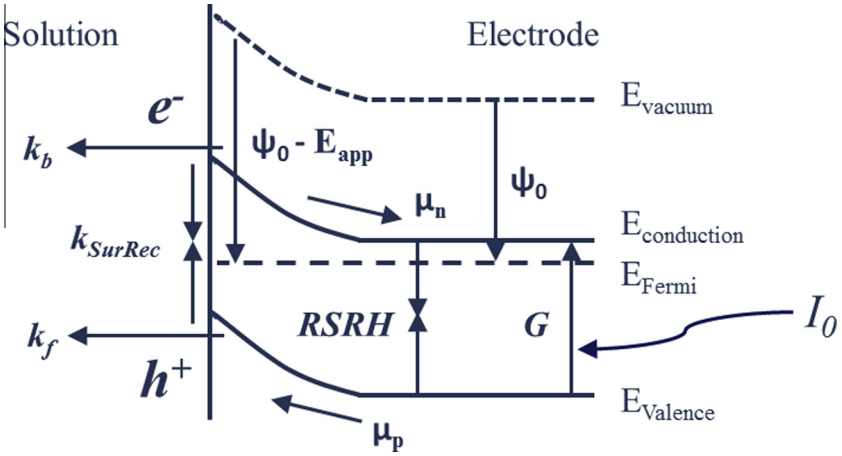

Fig. 1. Schematic diagram of reaction processes of excited electron and hole in the photoelectrodes. RSRH, the Shockley–Read-Hall recombination rate, indicates electron–hole recombination rate in the bulk semiconductor at steady-state (Eq. (6) in the text).

the trap-assisted Shockley–Read-Hall recombination equation was used in the simulations [29].

$$R = (C_n C_p - n_i^2)/(\tau_n(C_p + n_i) + \tau_p(C_n + n_i)) \quad (6)$$

where n_i is the intrinsic doping density and τ_n and τ_p is the recombination lifetime of electrons and holes. Also, the surface recombination of electrons and holes was considered as

$$dC_n/dt = dC_p/dt = -k_{\mathrm{SurRec}} C_n C_p \quad \text{(at the electrode surface)} \quad (7)$$

where k_{SurRec} is the rate constant of the surface trap recombination. G in Eqs. (3) and (4) is a generation rate of the charge carriers by the absorbed photon energy.

$$G = I_0 \alpha \exp(-\alpha x) \quad (8)$$

where α is the absorption coefficient of the photoanode, and I_0 is the incidence rate of photon. x is the penetration depth of the photon into the electrode. Initial conditions for ψ, C_n, and C_p were

$$\psi_0 = kT/q(\ln(C_{n0}/n_i) - \chi_{\mathrm{semi}} - 0.5E_g) \quad (9)$$

$$C_{n0} = n_d/2 + (n_d^2/4 + n_i^2)^{0.5} \quad (10)$$

$$C_{p0} = n_i^2/C_{n0} \quad (11)$$

where χ_{semi} is the electron affinity of semiconductor electrode, and E_g is the band gap energy of the semiconductor. The density of available states (n_s) was set to obtain the intrinsic doping density (n_i) of photoelectrodes (Eq. (12)). The donor density (n_d) of $BiVO_4$ was determined from the previously reported experimental values [5].

$$n_i = n_s \exp(-qE_g/2kT) \quad (12)$$

Boundary conditions for ψ, C_n, and C_p at the solution/electrode interface and at the electrode/metal contact were

$$\psi_{\mathrm{solution}} = \psi_0 - E_{\mathrm{app}} \quad (13)$$

$$dC_{n\_\mathrm{solution}}/dx = -k_b C_n C_B - k_{\mathrm{SurRec}} C_n C_p \quad (14)$$

$$dC_{p\_\mathrm{solution}}/dx = -k_f C_p C_A - k_{\mathrm{SurRec}} C_n C_p \quad (15)$$

$$\psi_{\mathrm{metal}} = \psi_0 \quad (16)$$

$$C_{n\_\mathrm{metal}} = C_{n0} \quad (17)$$

$$C_{p\_metal} = C_{p0} \quad (18)$$

where E_{app} is the applied potential, and k_f and k_b are the hole and electron transfer rate constants of reactions (19) and (20). C_A and C_B are the molecular concentrations of A and B in the solution.

$$A + h^+ \rightarrow C \quad (k_f) \quad (19)$$

$$B + e^- \rightarrow D \quad (k_b) \quad (20)$$

The chemical species, i.e., A and B, were treated as the sulfite and the dissolved oxygen in the solution. C_A and C_B were assumed as a constant and the reaction rates of (19) and (20) were limited by the electron and hole fluxes at the electrode surface. Then, linear sweep voltammograms (LSVs) of the photoelectrode were simulated as the E_{app} was changed from 0 to 1 V. The photocurrent (i) was calculated from the electron and hole flux at the electrode/metal interface.

$$i = q(dC_p/dx - dC_n/dx) \quad (21)$$

3. Results and discussion

3.1. Experiments with RG-O/$BiVO_4$

The photoactivity of $BiVO_4$ and RG-O/$BiVO_4$ composite electrodes were compared under the same conditions for sulfite oxidation as shown in Fig. 2a. For the RG-O/$BiVO_4$ electrode, 5 wt% of G-O was added to the precursor solution of $BiVO_4$ during electrode preparation. The optimum concentration of RG-O in the composite electrode was determined by varying the amount of G-O in the precursor solution and the results are shown in Fig. 3a. 5 wt% G-O in the precursor solution corresponds to 14 μg cm^{-2} of G-O in the prepared $BiVO_4$ electrode. As shown in Fig. 3, the photoactivity of the resulting RG-O/$BiVO_4$ was greatly affected by small changes in the G-O concentration in the precursor solution. Note that the weight ratio of G-O is based on the amount of G-O prepared in the precursor solution of the metal salts, and is the ratio of G-O to the total amount of G-O and resulting metal oxide from the metal salts. The amount of RG-O in the resulting electrode is reduced after the thermal annealing process used for electrode fabrication (see TGA results in Supporting information Fig. S2). However, the RG-O/$BiVO_4$ electrode prepared from 5 wt% G-O precursor solution showed several times higher photocurrent for sulfite oxidation both under UV–visible and visible light irradiation compared to that of $BiVO_4$ (see Supporting information Fig. S3 for response to visible light irradiation). As shown below in the finite element analysis, thermally reduced G-O facilitates the transfer of photoex-

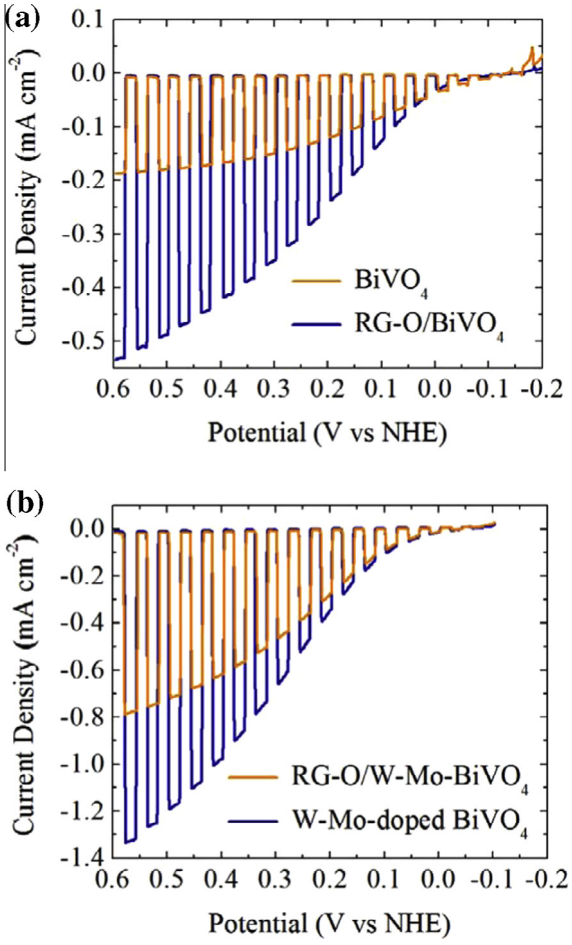

Fig. 2. LSV of (a) $BiVO_4$ (yellow) and RG-O/$BiVO_4$ (blue) and (b) W–Mo-doped $BiVO_4$ (blue) and RG-O/W–Mo-doped $BiVO_4$ (yellow) for sulfite oxidation in 0.1 M Na_2SO_3 and 0.1 M Na_2SO_4 aqueous solution (pH 7, 0.2 M sodium phosphate buffered). Scan rate was 20 mV s^{-1} and photocurrent was measured under chopped UV–visible irradiation. Beam intensity was about 120 mW cm^{-2}. (For interpretation of the references to color in this figure legend, the reader is referred to the web version of this article.)

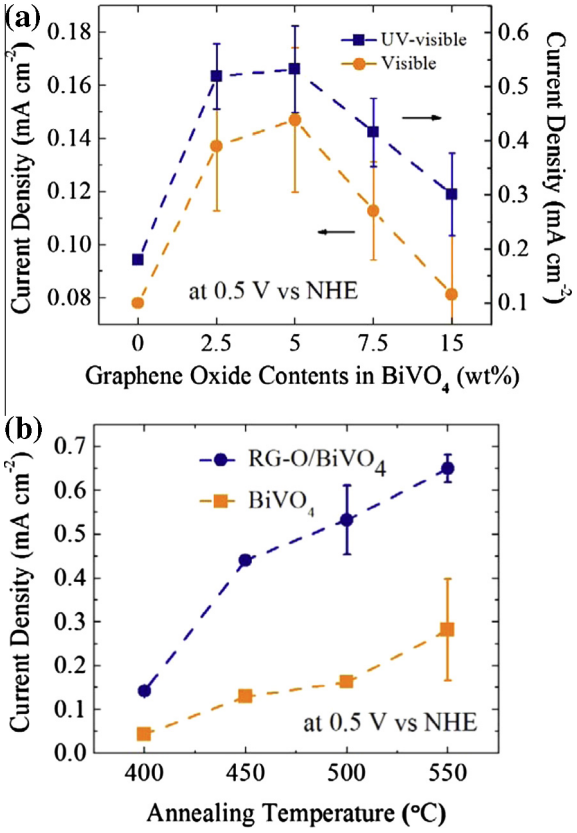

Fig. 3. Photocurrent dependence of RG-O/$BiVO_4$ composite electrode on the weight ratio of G-O to $BiVO_4$ for sulfite oxidation (a) and on the annealing temperature on photocurrent of RG-O/$BiVO_4$ composite electrode for sulfite oxidation (b). RG-O/$BiVO_4$ composite electrodes were drop-casted on FTO and annealed at 500 °C for 3 h in air in (a). The amount of G-O in the precursor solution was 5 wt% of the resulting $BiVO_4$ in (b) and RG-O/$BiVO_4$ composite electrodes were annealed at various temperatures for 3 h in air. The photocurrent was measured at 0.5 V (vs. NHE) in 0.1 M Na_2SO_3 and 0.1 M Na_2SO_4 aqueous solution under UV–visible irradiation. Note that the weight ratio of G-O is based on the G-O prepared in the precursor solution of metal oxide, and the weight ratio of RG-O in the resulting electrode is likely changed during the thermal process used for fabricating the electrodes.

cited electrons to the back contact, conductive FTO, so the incorporation of RG-O into the photocatalyst results in an improved separation of the excited electron–hole pairs [15].

As known from earlier studies [5] the annealing in air oxidatively converts the metal salts to $BiVO_4$. However, in this case it also leads to reduction of G-O with either the ethylene glycol or C acting as the reducing agents. The annealing temperature used for the preparation of RG-O/$BiVO_4$ composite electrodes was also varied (from 400 °C to 550 °C) to observe the effect on the photoactivity of RG-O/$BiVO_4$ for sulfite oxidation (Fig. 3b). The results show that RG-O/$BiVO_4$ or $BiVO_4$ fabricated at 400 °C has a far lower photoactivity, i.e., three times lower photocurrent at 0.5 V compared to those annealed at temperatures above 450 °C. The lower photocurrent of the composite electrodes prepared at 400 °C originated from the low photoactivity of tetragonal scheelite-like $BiVO_4$. The XRD pattern, shown in Supporting information Fig. S4, indicates that tetragonal scheelite-like $BiVO_4$ is formed in RG-O/$BiVO_4$ for the annealing temperature of 400 °C, but the peaks from this tetragonal phase are not observed in RG-O/$BiVO_4$ at annealing temperatures above 450 °C as shown in Fig. 4. Monoclinic scheelite-like $BiVO_4$, with a smaller band gap of 2.4 eV, is much more photoactive than the tetragonal scheelite-like $BiVO_4$ (band gap of 2.9 eV) [30]. In addition, TGA analysis in Supporting information

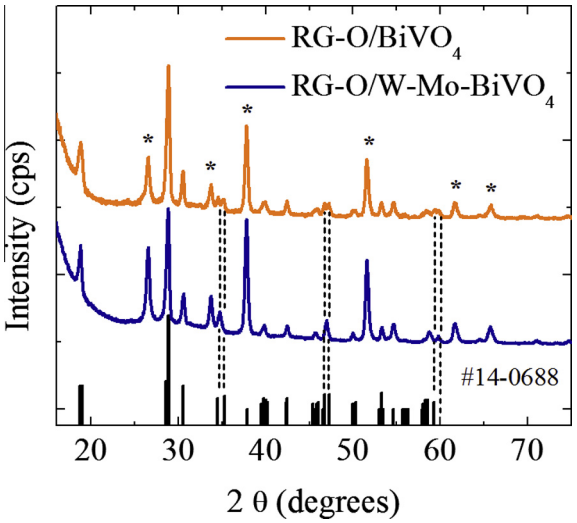

Fig. 4. XRD patterns of RG-O/$BiVO_4$ (yellow) and RG-O/W–Mo-doped $BiVO_4$ (blue). The reference patterns of the monoclinic scheelite-like $BiVO_4$ (PDF#14-0688, bottom line) and patterns from FTO substrate (*) are also indicated. Dotted lines indicate the characteristic shift of peaks from undoped $BiVO_4$ to the W–Mo-doped $BiVO_4$. (For interpretation of the references to color in this figure legend, the reader is referred to the web version of this article.)

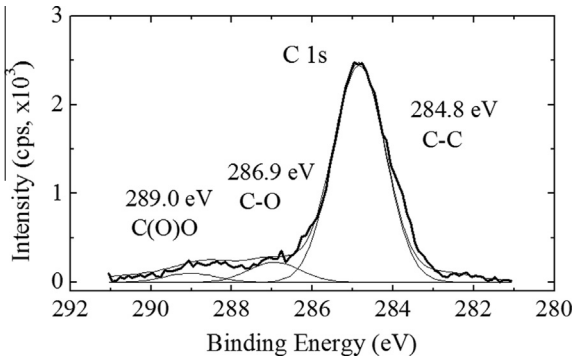

Fig. 5. XPS spectra for C1s of RG-O/$BiVO_4$ composite electrodes. The RG-O/$BiVO_4$ was prepared from 5 wt% G-O precursor solution on the FTO substrate. The drop-cast film was annealed at 500 °C for 3 h in air. Note that peaks are shifted (+1 eV) to compensate the sample charging effect in the XPS.

Fig. S2 shows that G-O is thermally reduced at temperatures of about 150 °C and both 400 °C and 450 °C are well above the temperature required for thermal reduction of G-O. XPS spectra for C1s of RG-O/$BiVO_4$ shown in Fig. 5 indicate that the G-O in the precursor solution is being reduced at the elevated temperatures (see Supporting information Fig. S5 for survey scan) [31]. However, further work is needed to study the chemistry of thermal reduction of G-O in air atmosphere and chemical environments used here, i.e., ethylene glycol. In summary, the photoactivity of RG-O/$BiVO_4$ composite is greatly affected by the properties of the host $BiVO_4$. Also, XRD measurements show that RG-O does not disrupt the formation of the $BiVO_4$ crystal structure for the simple drop-casting method. With properly prepared $BiVO_4$, the increased photoactivity of the RG-O composite electrodes indicates that RG-O is an excellent additive for the drop-cast $BiVO_4$ to improve the photocatalytic activity.

3.2. Experiments with RG-O/W–Mo-doped $BiVO_4$

RG-O composite electrodes with W–Mo-doped $BiVO_4$ were also prepared. W–Mo-doped $BiVO_4$ is a photocatalyst with several times greater photoactivity for water oxidation than undoped $BiVO_4$ [5]. Enhanced separation of excited electron–hole pairs has been suggested as a reason for the improved photoactivity of W–Mo-doped $BiVO_4$. Briefly, the modified electronic structure of $BiVO_4$ by doping W and Mo with a small shift of the flat band potential increases the electron (or hole) transfer in $BiVO_4$ [5]. To determine if a further improvement of photoactivity of the W–Mo-doped $BiVO_4$ could be realized, an RG-O composite electrode of W–Mo-doped $BiVO_4$ (RG-O/W–Mo-doped $BiVO_4$) was prepared from a solution of 5 wt% G-O and metal salts in ethylene glycol. Again note, RG-O does not affect the crystal formation of drop-cast W–Mo-doped $BiVO_4$ as shown by the XRD (Fig. 4). In other words, XRD patterns of RG-O/W–Mo-doped $BiVO_4$ show the peaks from monoclinic scheelite-like $BiVO_4$ along with characteristic peak shifts caused by the tetragonal deformation of the monoclinic scheelite-like $BiVO_4$ by the doping with W and Mo at 35, 47, and 59° in Fig. 4. However, the observed photoactivity of RG-O/W–Mo-doped $BiVO_4$ was smaller than that of W/Mo-doped $BiVO_4$ without RG-O (Fig. 2b). Photocurrent for sulfite oxidation measured at 0.5 V decreased about 40% from 1.7 mA cm^{-2} to 1.0 mA cm^{-2} by the addition of RG-O to W–Mo-doped $BiVO_4$ under UV–visible irradiation (see Supporting information Fig. S3 for visible response). The effects of the annealing temperature on the photoactivity were also studied for the RG-O/W–Mo-doped $BiVO_4$ at temperatures ranging from 450 °C to 550 °C (Supporting information Fig. S6) and RG-O/W–Mo-doped $BiVO_4$ shows lower photocurrent than W–Mo-doped $BiVO_4$ at all temperatures. The decrease of photoactivity of RG-O/W–Mo-doped $BiVO_4$ may imply that RG-O generates a recombination center or electron trap in W–Mo-doped $BiVO_4$. Also, the results indicate that the increased photocurrent of RG-O/$BiVO_4$ from $BiVO_4$ is not due to the increased electrode area or morphological changes of the photoelectrode; if the enhanced photoactivity of RG-O/$BiVO_4$ was due to the increased surface area of $BiVO_4$ as shown in the SEM images (Supporting information Fig. S7), a similar effect would also be seen for RG-O/W–Mo-doped $BiVO_4$.

It is established in sulfite oxidation that the incorporation of RG-O into $BiVO_4$ improves the photoactivity of undoped $BiVO_4$ as described above. There has also been a report of the improved PEC water oxidation on RG-O/$BiVO_4$ composite electrodes [16]. However, we found that the photocurrent measured for water oxidation showed that the increase of photocurrent by RG-O addition to $BiVO_4$ is less marked for water oxidation than that for sulfite oxidation (Fig. 6a). The enhancement of photocurrent for water oxidation by RG-O addition to $BiVO_4$ was only about 30% at the potential of 0.6 V from 30 μA cm^{-2} to 40 μA cm^{-2}. Although there is a report of very large increases in photocurrent by addition of RG-O to $BiVO_4$ from a few μA cm^{-2} to tens of μA cm^{-2} for water oxidation [16], we have not seen such a large effect. The smaller improvement of photocurrent with RG-O addition to $BiVO_4$ can be caused

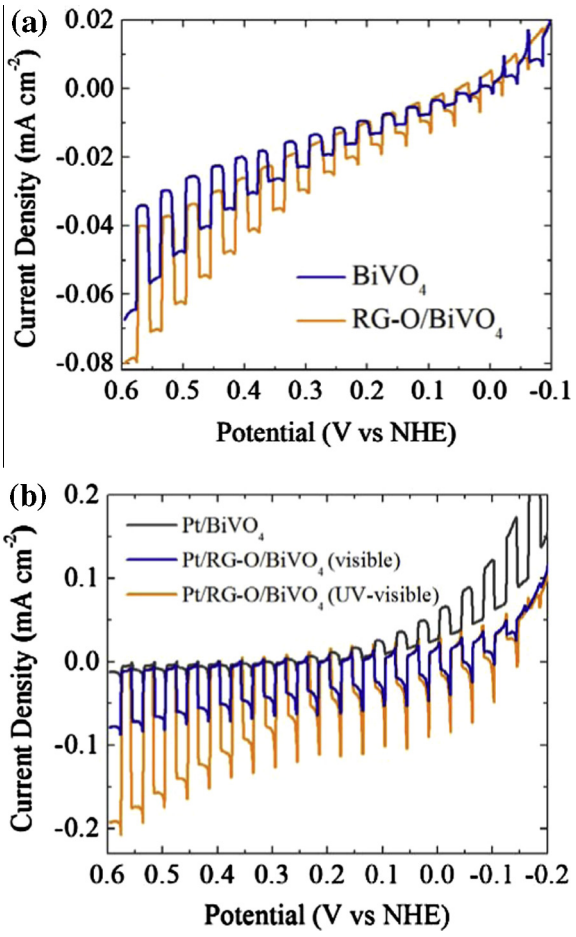

Fig. 6. LSVs of (a) $BiVO_4$ (blue) and RG-O/$BiVO_4$ (yellow) and (b) Pt/$BiVO_4$ (black) and Pt/RG-O/$BiVO_4$ (blue under visible and yellow under UV-visible irradiation) with photodeposited Pt electrocatalyst for water oxidation in 0.1 M Na_2SO_4 aqueous solution (pH 7, 0.2 M sodium phosphate buffered). Scan rate was 20 mV s^{-1}. Photocurrent was measured under chopped UV–visible irradiation. Beam intensity was about 120 mW cm^{-2}. (For interpretation of the references to color in this figure legend, the reader is referred to the web version of this article.)

by the slower kinetics of inner-sphere reactions of water oxidation compared with the fast and irreversible sulfite oxidation. In other words, slow charge transfer at the surface from the photocatalyst to the adsorbate is the rate-determining step of photo-induced water oxidation. Improvement in bulk carrier mobility does not help in the effective separation of electron–hole pairs of RG-O/$BiVO_4$ for water oxidation; yet is obvious for the fast sulfite oxidation. In addition, for W–Mo-doped $BiVO_4$ the negative effect of RG-O on the photoactivity of W–Mo-doped $BiVO_4$ was also confirmed in water oxidation (not shown here).

3.3. Experiments with Pt Electrocatalyst on RG-O/$BiVO_4$

To increase the kinetics of water oxidation on $BiVO_4$ and RG-O/$BiVO_4$, a Pt electrocatalyst was photodeposited onto the electrodes [32]. The results in Fig. 6b shows that for water oxidation the photooxidation current of RG-O/$BiVO_4$ increased about five times by the addition of Pt catalyst from 40 $\mu A\,cm^{-2}$ to 200 $\mu A\,cm^{-2}$ at 0.6 V. In contrast to RG-O/$BiVO_4$, $BiVO_4$ without RG-O exhibited no improvement from the catalyst. Pt/$BiVO_4$ actually showed slightly lower currents than the film without the electrocatalyst. This suggests that $BiVO_4$ without G-O still suffers from severe electron–hole recombination that limits the overall rate of the reactions. However, it is also possible that the Pt electrocatalysts were not properly photodeposited on $BiVO_4$ without G-O as the $BiVO_4$ shows poorer photoactivity than RG-O/$BiVO_4$ under the given experimental conditions.

3.4. Digital simulations

Finite element analysis was performed to study the effects of addition of RG-O to $BiVO_4$. Experimental results shown in Fig. 2 for sulfite oxidation of $BiVO_4$ were used to fit the simulation parameters, i.e., the hole and electron transfer rate constants (k_f and k_b in Eqs. (14) and (15)), the surface recombination rate constants (k_{SurRec}), the electron and hole mobility (μ_n and μ_p), and the electron and hole recombination lifetimes (τ_n and τ_p) of $BiVO_4$.

The simulated LSVs of $BiVO_4$, R-GO/$BiVO_4$ and W–Mo-doped $BiVO_4$ electrodes are shown in Fig. 7 with the experimental results. The fitting parameters obtained from simulations are summarized in Tables 1 and 2. The parameters were assigned for the model used and the values are largely determined by the specific calculations in this study. Thus, experiments that are independent of the PEC ones that can provide accurate parameters, such as mobility, are still required to ensure a unique set of properties in the given model. To show the sensitivity of fitting parameters in the model used, simulated LSVs for $BiVO_4$ are shown with varied values for four different parameters in Supporting information Fig. S8. In the calculations for the $BiVO_4$, carrier mobility and lifetime affected the photocurrent densities over wide potential ranges where the rate constants for surface recombination reaction (7) and electro-

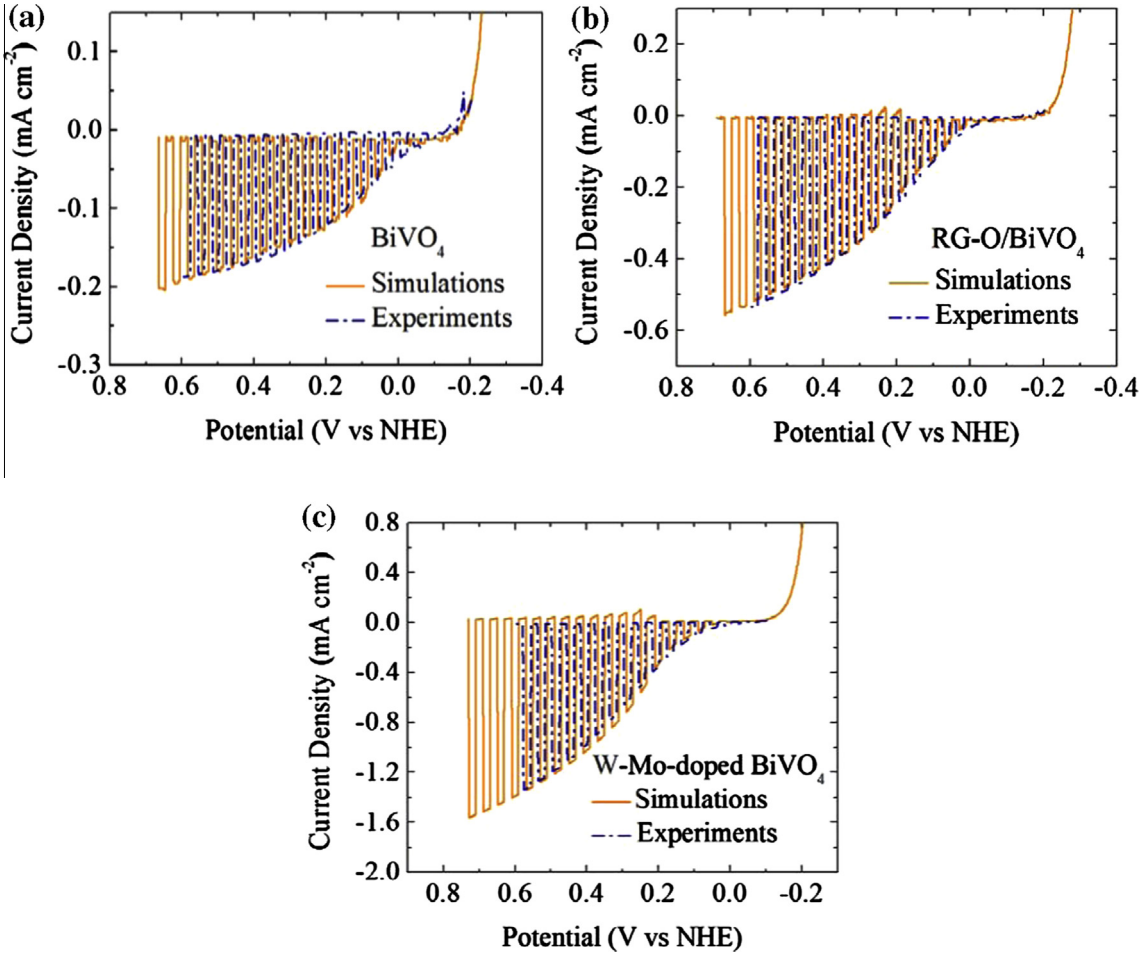

Fig. 7. Comparison of simulated LSVs (yellow solid) to experimental results (blue dash) of (a) $BiVO_4$, (b) RG-O/$BiVO_4$, and (c) W–Mo-doped $BiVO_4$. The experimental results were taken from Fig.2 for sulfite oxidation under UV–visible irradiation. Scan rate was 20 mV s^{-1}. Parameters used for simulation fitting were summarized in Table 1 and Supporting information Table S1. (For interpretation of the references to color in this figure legend, the reader is referred to the web version of this article.)

Table 1
Simulation input parameters for $BiVO_4$, R-GO/$BiVO_4$, and W–Mo–$BiVO_4$ electrodes shown in Fig. 7. *The donor doping density (n_d) of W–Mo–$BiVO_4$ that is larger than $BiVO_4$ has been reported and the W–Mo–$BiVO_4$ may also have larger intrinsic doping density (n_i) than $BiVO_4$ with the higher doping level of W and Mo into $BiVO_4$. However, n_i was fixed as a constant for the simulations in Fig. 7 for all the electrodes that resulted in the lower n_d for W/Mo-doped $BiVO_4$ than $BiVO_4$. (H.S. Park, K.E. Kweon, H. Ye, E. Paek, G.S. Hwang, A.J. Bard, J. Phys. Chem. C, 115 (2011) 17870–17879.)

Parameter	Value			Units	Description
	BiVO4	RG-O/BiVO4	W–Mo-BiV04		
μ_n	12	150	300	$cm^2\ V^{-1}\ s^{-1}$	Electron mobility
μ_p	2	35	100	$cm^2\ V^{-1}\ s^{-1}$	Hole mobility
τ_n	0.25	0.14	0.33	ps	Electron lifetime
τ_p	0.25	0.14	0.33	ps	Hole lifetime
n_d^*	4×1019	4×10^{18}	1×10^{17}	cm^{-3}	Donor doping density
k_f	8×10^{-17}	8×10^{-17}	1.2×10^{-16}	$cm^3\ s^{-1}$	Rate constant of reaction (19)
k_b	4×10^{-20}	1×10^{-21}	4×10^{-20}	$cm^3\ s^{-1}$	Rate constant of reaction (20)
k_{SurRec}	1×10^{-4}	2×10^{-5}	1×10^{-4}	$cm^4\ s^1$	Rate constant of reaction (7)
$E_{FlatBand}$	−0.53	−0.41	−0.31	V	Flat band potential vs NHE at pH 7

Table 2
Values calculated from input parameters shown in Table 1.

Parameter	Value			Units	Description
	BiVO4	RG-O/BiVO4	W–Mo-BiV04		
D_n	3.1×10^{-1}	3.8	7.8	$cm^2\ s^{-1}$	Electron diffusion coefficient
D_p	5.2×10^{-2}	9.0×10^{-1}	2.6	$cm^2\ s^{-1}$	Hole diffusion coefficient
L_n	2.8	7.3	16	nm	Electron diffusion length
L_p	1.1	3.5	9.3	nm	Hole diffusion length

chemical reaction (19) showed limited effects near the onset potentials. However, the values given are still useful as relative measures of the properties of the systems investigated here. Thus the electron and hole diffusion lengths ($L_{n/p}$) calculated from its diffusion coefficient and recombination lifetime was 2.8 and 1.1 nm for BiVO $_4$, respectively.

$$L_{n/p} = (D_{n/p} \times \tau_{n/p})^{0.5} \quad (22)$$

The recombination lifetime (~1 ps) and diffusion length (~2 nm) of $BiVO_4$ are similar to that reported for α-Fe_2O_3 which results in poor photoactivity [33]. However, as the RG-O was added to $BiVO_4$, it provided a better channel for electron transport that increased the electron and hole mobility and the diffusion length. The electron and hole diffusion length increased about three times from 2.8 and 1.1 nm to 7.3 and 3.5 nm with the addition of RG-O to $BiVO_4$ (Table 2). The electron and hole diffusion length of W–Mo-doped $BiVO_4$ was even longer than RG-O/$BiVO_4$ as expected from the measured photocurrent in Fig. 2 (16 and 9.3 nm). However, the obtained electron/hole recombination lifetime of photoelectrodes is extremely short, ~0.1 to 0.3 ps. For such an extremely short lifetime, the electrodes prepared by drop casting have many grain boundaries (SEM in Supporting information Fig. S7) that can introduce carrier traps and shorten the electron/hole recombination lifetime. The electron and hole diffusion lengths of $BiVO_4$, RG-O/$BiVO_4$, and W–Mo-doped $BiVO_4$ are still much smaller than, for example, that of TiO_2 (~10 μm) and have low fill factors in the current–potential behavior compared with the TiO_2 [34]. However, the digital simulations show that improved electron and hole mobility and lifetime by addition of RG-O or W/Mo into $BiVO_4$ results in less electron/hole recombination in the bulk semiconductor (Fig. 8a). The peak trap recombination rate of $BiVO_4$ electrode at 0.6 V (vs NHE) is $15 \times 10^{20}\ cm^{-3}\ s^{-1}$, and it decreases to $14 \times 10^{20}\ cm^{-3}\ s^{-1}$ and $12 \times 10^{20}\ cm^{-3}\ s^{-1}$ in the RG-O/$BiVO_4$ and W–Mo-doped $BiVO_4$ electrodes. As the recombination rate decreases, the net flux of minority carrier at the electrode surface increases from $1 \times 10^{15}\ cm^{-2}\ s^{-1}$ ($BiVO_4$) to 3×10^{16} (RG-O/$BiVO_4$) and $9 \times 10^{15}\ cm^{-2}\ s^{-1}$ (W/Mo-doped $BiVO_4$) as shown in Fig. 8b. The increased minority carrier flux and reduced recombination rates improves the photoactivity of the RG-O/$BiVO_4$ and W–Mo-doped $BiVO_4$.

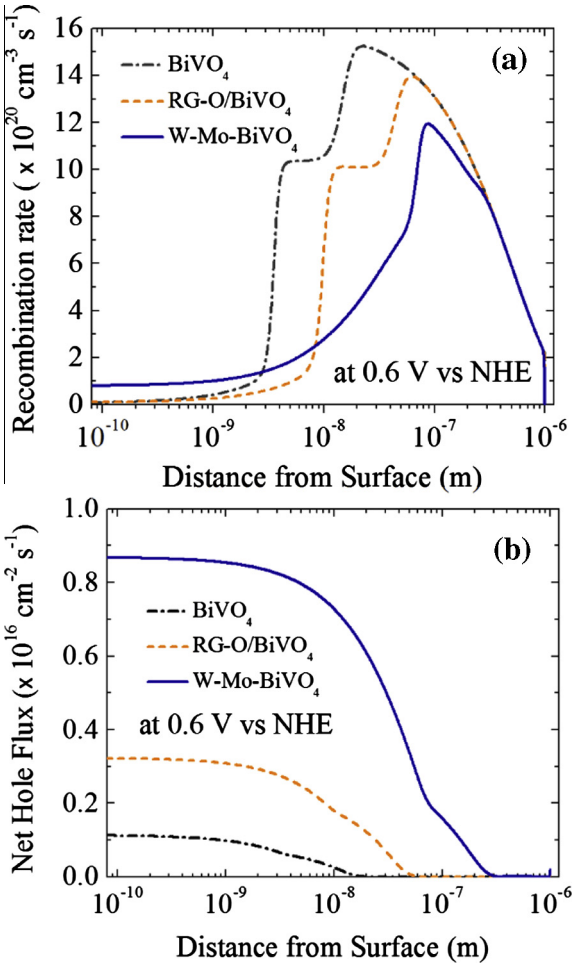

Fig. 8. (a) Recombination rate of electron–hole pairs and (b) net hole flux in $BiVO_4$ (black dash-dot), RG-O/$BiVO_4$ (yellow dash), and W–Mo-doped $BiVO_4$ (blue solid) electrodes from the calculation shown in Fig. 7. (For interpretation of the references to color in this figure legend, the reader is referred to the web version of this article.)

In summary, RG-O/$BiVO_4$ exhibited significantly improved photoactivity compared to $BiVO_4$ by the addition of RG-O. The results indicate that RG-O efficiently facilitates the electron–hole separation in $BiVO_4$ or reduced electron–hole recombination in the bulk electrodes. Moreover, metal doping of W and Mo into $BiVO_4$ shows a positive effect on the photoactivity of $BiVO_4$. The quantitative semiconductor properties were estimated using finite element analysis. In addition, an electrocatalyst, Pt, is required to improve the kinetics of water oxidation to realize the effect of reduced electron–hole recombination of the RG-O/$BiVO_4$ composite photocatalyst.

4. Conclusions

The photoactivity of the photocatalyst, $BiVO_4$, for sulfite oxidation was improved by about 3 times by the addition of RG-O. Presumably RG-O as a conductive channel of electrons reduces the electron–hole recombination rate, which is the main factor limiting high photoactivity of metal oxide photocatalysts. The improved carrier diffusion length, mobility, and reduced recombination rate by the addition of RG-O and W and Mo dopants into $BiVO_4$ were studied by digital simulations. As a result of the addition of RG-O and metal dopants, the electron and hole diffusion length increased from 2.8 and 1.1 nm ($BiVO_4$) to 7.3 and 3.5 nm (RG-O/$BiVO_4$) and 16 and 9.3 nm (W/Mo-doped $BiVO_4$). However, improved electron–hole separation was not significant for water oxidation on RG-O/$BiVO_4$ probably because of the kinetic limitations of the inner-sphere water oxidation surface reaction. Pt electrocatalyst was thus photodeposited onto RG-O/$BiVO_4$ to decrease the kinetic limitations. The resulting Pt/RG-O/$BiVO_4$ electrode showed several times higher photocurrent for water oxidation than Pt/$BiVO_4$ or $BiVO_4$.

Acknowledgments

We acknowledge the Samsung SAIT GRO Program, the US Department of Energy, Office of Basic Energy Sciences, Division of Materials Sciences and Engineering under Award DE-FG02-09ER16119, and the Robert A. Welch Foundation AJB F-0021 for financial support of this project.

Appendix A. Supplementary material

Supplementary data associated with this article can be found, in the online version at http://dx.doi.org/10.1016/j.jelechem.2013.08.036.

References

[1] B.D. Alexander, P.J. Kulesza, I. Rutkowska, R. Solarska, J. Augustynski, J. Mater. Chem. 18 (2008) 2298–2303.
[2] I. Cesar, A. Kay, J.A.G. Martinez, M. Gratzel, J. Am. Chem. Soc. 128 (2006) 4582–4583.
[3] B. Cole, B. Marsen, E. Miller, Y. Yan, B. To, K. Jones, M. Al-Jassim, J. Phys. Chem. C 112 (2008) 5213–5220.
[4] H. Ye, J. Lee, J.S. Jang, A.J. Bard, J. Phys. Chem. C 114 (2010) 13322–13328.
[5] H.S. Park, K.E. Kweon, H. Ye, E. Paek, G.S. Hwang, A.J. Bard, J. Phys. Chem. C 115 (2011) 17870–17879.
[6] J.A. Glasscock, P.R.F. Barnes, I.C. Plumb, N. Savvides, J. Phys. Chem. C 111 (2007) 16477–16488.
[7] J.H. Kennedy, K.W. Frese Jr., J. Electrochem. Soc. 125 (1978) 709–714.
[8] M.A. Butler, J. Appl. Phys. 48 (1977) 1914–1920.
[9] Y. Lin, S. Zhou, X. Liu, S. Sheehan, D. Wang, J. Am. Chem. Soc. 131 (2009) 2772–2773.
[10] S. Banerjee, S.K. Mohapatra, M. Misra, J. Phys. Chem. C 115 (2011) 12643–12649.
[11] R. Liu, Y. Lin, L.-Y. Chou, S.W. Sheehan, W. He, F. Zhang, H.J.M. Hou, D. Wang, Angew. Chem. Int. Ed. 50 (2011) 499–502.
[12] Y. Lin, S. Zhou, S.W. Sheehan, D. Wang, J. Am. Chem. Soc. 133 (2011) 2398–2401.
[13] S.K. Mohapatra, K.S. Raja, V.K. Mahajan, M. Misra, J. Phys. Chem. C 112 (2008) 11007–11012.
[14] Y.H. Ng, I.V. Linghtcap, K. Goodwin, M. Matsumura, P.V. Kamat, J. Phys. Chem. Lett. 1 (2010) 2222–2227.
[15] G. Williams, B. Seger, P.V. Kamat, ACS Nano 2 (2008) 1487–1491.
[16] Y.H. Ng, A. Iwase, A. Kudo, R. Amal, J. Phys. Chem. Lett. 1 (2010) 2607–2612.
[17] D.M. Fleetwood, P.S. Winokur, R.A. Reber Jr., T.L. Meisenheimer, J.R. Schwank, M.R. Shaneyfelt, L.C. Riewe, J. Appl. Phys. 73 (1993) 5058–5074.
[18] B.C. Brodie XIII, Philos. Trans. R. Soc. London 149 (1859) 249–259.
[19] D.R. Dreyer, S. Park, C.W. Bielawski, R.S. Ruoff, Chem. Soc. Rev. 39 (2010) 228–240.
[20] K.P. Loh, Q. Bao, G. Eda, M. Chhowalla, Nat. Chem. 2 (2010) 1015–1024.
[21] J.R. Potts, D.R. Dreyer, C.W. Bielawski, R.S. Ruoff, Polymer 52 (2011) 5–25.
[22] D.H. Lee, J.E. Kim, T.H. Han, J.W. Hwang, S. Jeon, S.-Y. Choi, S.H. Hong, W.J. Lee, R.S. Ruoff, S.O. Kim, Adv. Mater. 22 (2010) 1247–1252.
[23] M.D. Stoller, S. Park, Y. Zhu, J. An, R.S. Ruoff, Nano Lett. 8 (2008) 3498–3502.
[24] D. Laser, A.J. Bard, J. Electrochem. Soc. 123 (1976) 1828–1832.
[25] M.E. Orazem, J. Newman, J. Elctrochem. Soc. 131 (1984) 2574–2582.
[26] S.J. Anz, N.S. Lewis, J. Phys. Chem. B 103 (1999) 3908–3915.
[27] W.S. Hummers Jr., R.E. Offeman, J. Am. Chem. Soc. 80 (1958) 1339.
[28] B. Kraeutler, A.J. Bard, J. Am. Chem. Soc. 100 (1978) 4317–4318.
[29] J.M. Foley, M.J. Price, J.I. Feldblyum, S. Maldonado, Energy Environ. Sci. 5 (2012) 5203–5220.
[30] S. Tokunaga, H. Kato, A. Kudo, Chem Mater. 13 (2001) 4624–4628.
[31] D. Yang, A. Velamakanni, G. Bozoklu, S. Park, M. Stoller, R.D. Piner, S. Stankovich, I. Jung, D.A. Field, C.A. Ventrice Jr., R.S. Ruoff, Carbon 47 (2009) 145–152.
[32] H. Ye, H.S. Park, A.J. Bard, J. Phys. Chem. C. 115 (2011) 12464–12470.
[33] D.A. Wheeler, G. Wang, Y. Ling, Y. Li, J.Z. Zhang, Energy Environ. Sci. 5 (2012) 6682–6702.
[34] W.H. Leng, P.R.F. Barnes, M. Juozapavicius, B.C. O'Regan, J.R. Durrant, J. Phys. Chem. Lett. 1 (2010) 967–972.